Geol. Mag. **154** (3), 2017, pp. 441–455. © Cambridge University Press 2016
doi:10.1017/S0016756816000054

Age and tectonic setting of the East Taiwan Ophiolite: implications for the growth and development of the South China Sea

ROBERT B.-J. HSIEH, J. GREGORY SHELLNUTT* & MENG-WAN YEH

National Taiwan Normal University, Department of Earth Sciences, 88 Tingzhou Road Section 4, Taipei 11677, Taiwan

(*Received* 21 September 2015; *accepted* 8 January 2016; *first published online* 10 May 2016)

Abstract – The South China Sea is one of the youngest marginal seas and understanding its development is important for reconstructing the tectonic evolution of Southeast Asia. The South China Sea is thought to have been actively spreading between 32 Ma and 15.5 Ma. The East Taiwan Ophiolite (ETO) is one of the few preserved remnants of the South China Sea on land and provides an opportunity to investigate the age and the tectonic setting of the accreted easternmost portion. The age of the ETO was obtained by LA-ICP-MS *in situ* zircon U–Pb methods and yielded a mean ^{206}Pb–^{238}U age of 14.1 ± 0.4 Ma, suggesting that magmatic activity in the South China Sea continued ~1.5 million years beyond current estimates. Cr-spinel data (Cr no. = 42–54) and depleted $\varepsilon_{Nd}(t)$ values (i.e. +9.1 to +11.4) from the serpentinized peridotites and gabbros and the light rare earth element depleted patterns (La/Yb ≤ 1) of the ETO mafic rocks are consistent with a ridge setting (i.e. N-MORB composition). Therefore, the ETO likely represents the terminal portion of the South China Sea spreading ridge that was sheared off during the northward translation of the Luzon arc.

Keywords: South China Sea, East Taiwan Ophiolite, Cr-spinel, mid-ocean ridge, serpentinized peridotite.

1. Introduction

The South China Sea (SCS) is one of the youngest marginal ocean basins bordered by the South China Block, Indochina Block, Luzon arc and Palawan, and is an important feature for reconstructing the Cenozoic tectonic evolution of Southeast Asia (Fig. 1a) (Taylor & Hayes, 1980; Tapponnier *et al.* 1990; Briais, Patriat & Tapponnier, 1993; Lee & Lawver, 1995; Flower, Tamaki & Hoang, 1998; Zhang, Xiong & Wang, 2001; Barckhausen & Roeser, 2004; Xia *et al.* 2005; Barckhausen *et al.* 2014; Li *et al.* 2014). The spreading of the South China Sea began from early Oligocene time and continued until early–middle Miocene time (~32 to ~15.5 Ma), according to magnetic anomaly mapping (anomalies 11 to 5d, Taylor & Hayes, 1980, 1983; revised to anomalies 11 to 5c, Briais, Patriat & Tapponnier, 1993). Although the final spreading time of the South China Sea is considered to range between 10 Ma and 15 Ma according to seismic stratigraphic data of several sub-basins (Franke *et al.* 2014), Arfai *et al.* (2011) indicated that the onset of the subduction of the South China Sea oceanic plate under the Manila Trench in the east marked the cessation of sea-floor spreading. Coincident 15 Ma geological features such as the commencement of the volcanic belt along western Luzon (Pubellier *et al*. 2000), and the beginning of the Palawan/Mindoro–Central Philippines collision (Yumul *et al.* 2003) are seen as supporting evidence for the age determination for the cessation of South China Sea sea-floor spreading, and is further implied as the timing for subduction of the oldest crust. However, there is no evidence that sea-floor spreading did not continue after the initial onset of subduction as a considerable portion of the inferred oceanic crust was subducted.

Accessible remnants of the South China Sea are preserved within the Lichi mélange of the Coastal Range in eastern Taiwan. These oceanic rocks consist of fragments of fossiliferous sea-floor sediments, pillow basalt, glassy basalt, gabbro, basaltic dykes, plagiogranite and serpentinized peridotite, and are known as the East Taiwan Ophiolite (ETO) (Liou *et al.* 1977; Jahn, 1986; Chung & Sun, 1992). The nature and tectonic setting of the ETO is a topic that is still under debate (Suppe, Liou & Ernst, 1981; Jahn, 1986; Chung & Sun, 1992; W. Y. Shao, unpub. Ph.D. thesis, National Taiwan Univ., 2015). Based on the stratigraphy of the Lichi Formation, Suppe, Liou & Ernst (1981) suggested that the ETO is a submarine scree deposit consisting of angular mafic and ultramafic plutonic blocks that formed at a 'leaky' transform fault offset. Jahn (1986), however, interpreted the ETO as a spreading ridge from an open ocean or marginal basin based upon the geochemical and isotopic data of the glassy basalts, gabbros and plagiogranites, whereas Chung & Sun (1992) proposed the ETO formed in a slow-spreading ridge environment.

The bulk-rock geochemistry and mineral geochemistry of oceanic peridotites can be used to distinguish between different tectonic settings (Dick & Bullen, 1984; Bonatti & Michael, 1989; Arai, 1992, 1994; Kamenetsky, Crawford & Meffre, 2001; Hebert *et al.* 2003). Some major and trace elements such as Mg, Cr and Al, which are relatively immobile during serpentinization, can retain their original concentration and thus help to identify the possible tectonic setting.

*Author for correspondence: jgshelln@ntnu.edu.tw

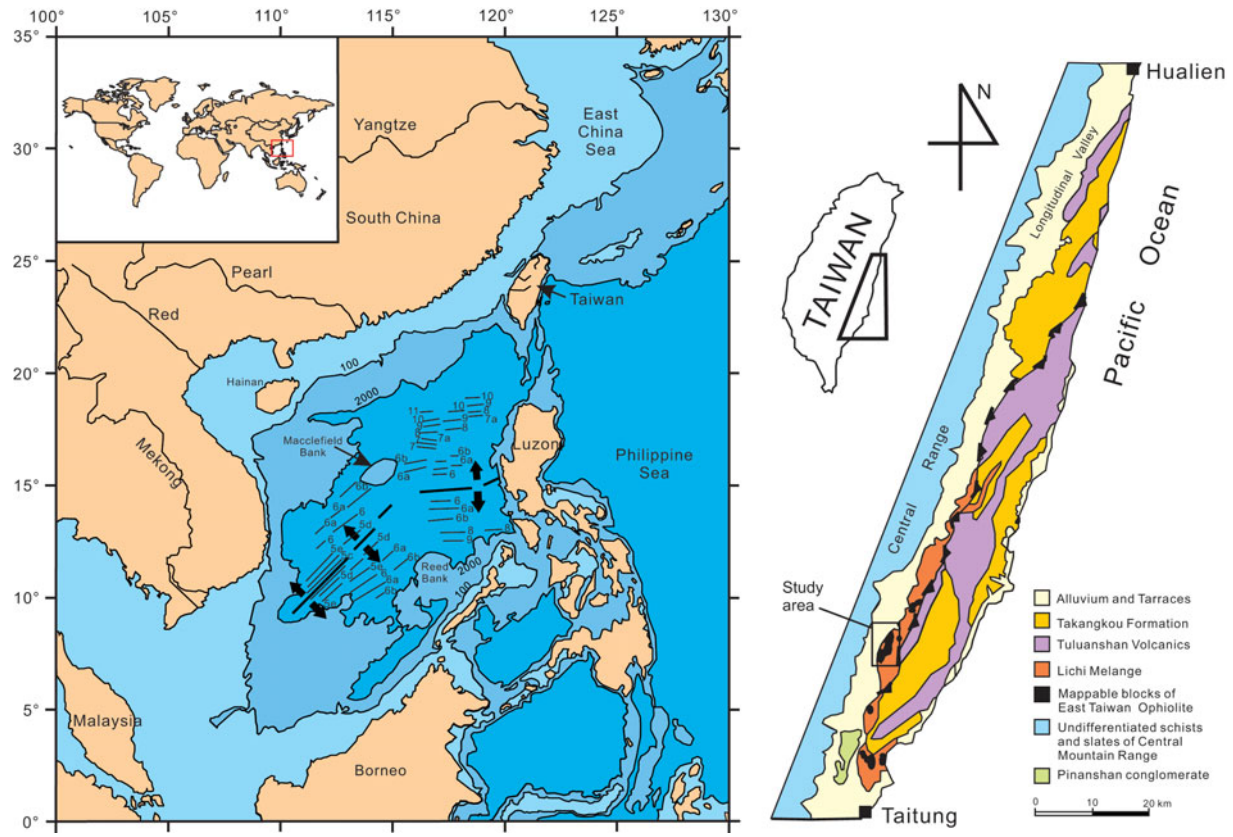

Figure 1. (a) Map of the South China Sea, Southeast Asia and (b) the location of the ETO. Simplified geological map of the Coastal Range region of Taiwan (revised from Liou, 1979).

New spinel mineral chemistry, whole-rock major and trace elemental data and Sr–Nd isotopes of the serpentinized peridotites and an *in situ* zircon U–Pb date of a hornblende gabbro are presented in order to constrain the tectonic setting and age of the ETO within the context of the regional tectonic development of the South China Sea.

2. Geological and tectonic background

Taiwan is situated at the junction between the Ryukyu arc and the Luzon arc and is an amalgamation of accretionary wedge rocks, island arc rocks and older continental and oceanic lithosphere (Chai, 1972; Bowin *et al.* 1978; Suppe, 1984; Tsai, 1986; Kao, Shen & Ma, 1998). Westward subduction of the Pacific plate beneath the Eurasian plate during Mesozoic time (~150 Ma) created the Zhejiang–Fujian magmatic arc and proto-Taiwan. As subduction slowed during early Cenozoic time, the slab began to roll back eastwardly until the palaeo-Pacific plate eventually stopped subducting. The changing nature of convergence between the palaeo-Pacific plate and Eurasia allowed sediments to accumulate in a fore-arc basin setting as the Philippine Sea plate rotated clockwise in a northwestward direction (Lee & Lawver, 1995). During middle to late Miocene time (~15-12 Ma), the Luzon arc migrated towards the Eurasian continental shelf along a left-lateral transform fault compensating the northward subduction of the northern Philippine Sea plate under the Ryukyu arc (Teng, 1990; Huang, Yuan & Tsao, 2006). The obduction between the Luzon arc and Eurasian continental shelf uplifted the accretionary wedge as the proto-Central Mountain Range of Taiwan during mid to late Pliocene time (Teng, 1990; Huang, Yuan & Tsao, 2006). By late Pliocene time, the northern Luzon arc obliquely collided into Eurasia and reached its current position off the east coast of Taiwan. The volcanic rocks of the Luzon arc accreted to the uplifted Pliocene–Pleistocene passive margin sediments of Eurasia and became the Coastal Range, whereas the uplifted sedimentary rocks developed into the Central Range. Concurrent with the Luzon–Eurasia collision, NE Taiwan transformed from compression to extension as the Philippine Sea plate continue to subduct under the Ryukyu arc, which induced back-arc extension and the opening of the Okinawa Trough (Teng, 1990, 2007; Kao, Shen & Ma, 1998) and the Yilan basin by the collapsing of the Yilan terrane (Suppe, 1984; Lee & Wang, 1987; Teng, 1990, 1996, 2007).

The ~140 km long Coastal Range of eastern Taiwan is one of the five main mountain ranges of the island and stretches from the Hualien River in the north to Beinan Mountain in the south (Fig. 1b). The Coastal Range is separated into a slightly higher but no longer uplifting northern portion (Chen, Huang & Liu, 1991) and a lower but still uplifting southern portion with abundant river terraces cut by the Siouguluan River. The Longitudinal Valley situated between the Central Range and Coastal Range marks the boundary between

https://doi.org/10.1017/S0016756816000054 Published online by Cambridge University Press

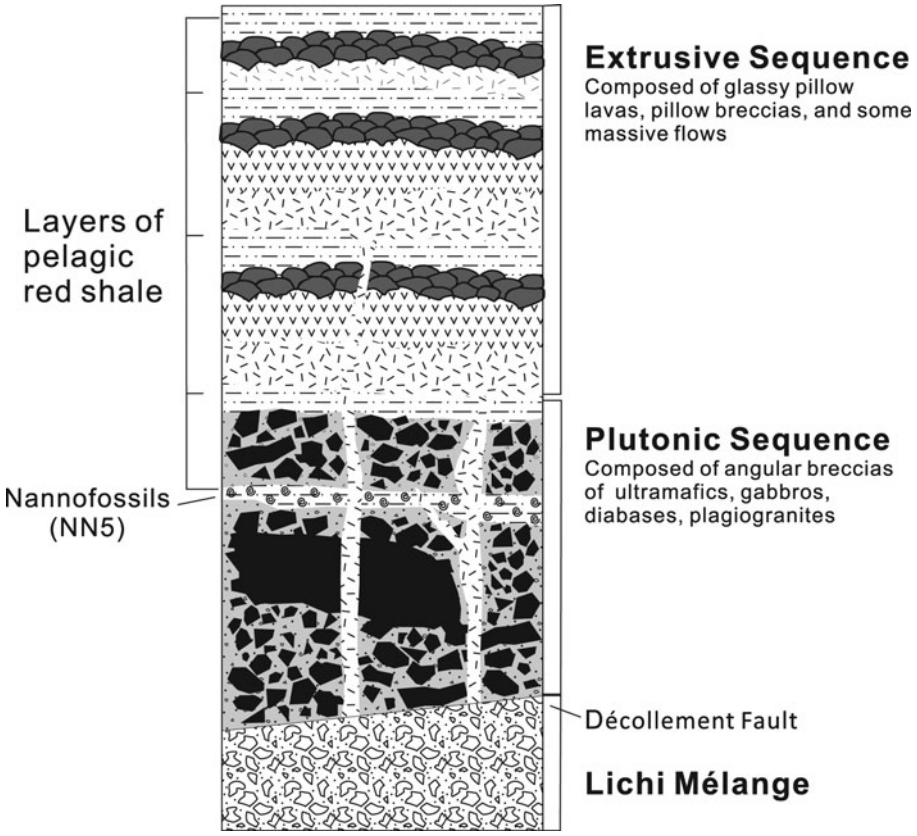

Figure 2. Idealized stratigraphy of the ETO (revised from Liou *et al.* 1977).

Eurasia and the Philippine Sea plate. The Central Range is underlain by deformed rocks of the Eurasian continental margin while the Coastal Range is underlain by island arc volcanic rocks from the Luzon arc (Pagé & Suppe, 1981).

The ETO is sporadically exposed along the southeastern part of the Coastal Range and is considered to be a remnant of the South China Sea (Liou *et al.* 1977; Suppe & Liou, 1979; Liou, 1979; Suppe, Liou & Ernst, 1981; Jahn, 1986; Chung & Sun, 1992). Liou *et al.* (1977) provided a detailed geological and geochemical investigation that interpreted the ETO as an ocean ridge. The interpretation by Liou *et al.* (1977) has since been modified and constrained into the current synthesis as shown in Figure 2 (Suppe, Liou & Ernst, 1981; Jahn, 1986; Chung & Sun, 1992). For this study, samples were collected at Dianguang, Guanshan Township, along the Chiawu creek that exposes the largest contiguous outcrop of the ETO. Rocks were collected along a 1.6 km traverse from midstream to the headwater. The serpentinized peridotites were collected near the headwater of the creek whereas the gabbro was collected closer to the start of the traverse.

3. Petrography

The peridotites mostly (≥ 90 vol. %) comprise serpentine with minor amounts of orthopyroxene pseudomorphs (≥ 5 vol. %) and spinel (≥ 1 vol. %). The original texture of the rock has been replaced but the serpentine suggests the rock was poikilitic. Small iron-oxide minerals form anastomosing bands which give the appearance of former grain boundaries. The oxide minerals are likely the result of olivine serpentinization. There are rare occurrences of partly altered (i.e. pseudomorphic?) olivine which range in size from 0.5 mm to ~1 mm and still have discernable hexagonal to rounded shapes. Orthopyroxene pseudomorphs range in size from 0.5 mm to 3.5 mm and represent ~5 % of the rock mode. The orthopyroxene pseudomorphs are commonly round and larger than the pseudomorphic olivine, have a distinct relief from the serpentine and still have visible cleavage that makes them relatively easy to identify. Subhedral to anhedral spinel is commonly observed and is between 0.5 and 2 mm in length and dark red in plain-polarized light (Fig. 3). Magnetite- and calcite-rich veins are common and are likely due to the hydrothermal alteration of the original silicate minerals.

The gabbro is coarse grained and granular and consists of ~55 % hornblende and ~45 % plagioclase with accessory quantities (i.e. < 1 vol. %) of ilmenite and/or magnetite. The hornblende is light green under plain-polarized light with second-order interference colours under crossed polars. The hornblende crystals are euhedral to subhedral and tend to be smaller (i.e. 0.1 mm) than the subhedral to anhedral plagioclase crystals (i.e. > 0.5 mm). The oxide minerals are small (i.e. < 0.05 mm), sub- to anhedral and commonly bordering plagioclase rather than hornblende.

https://doi.org/10.1017/S0016756816000054 Published online by Cambridge University Press

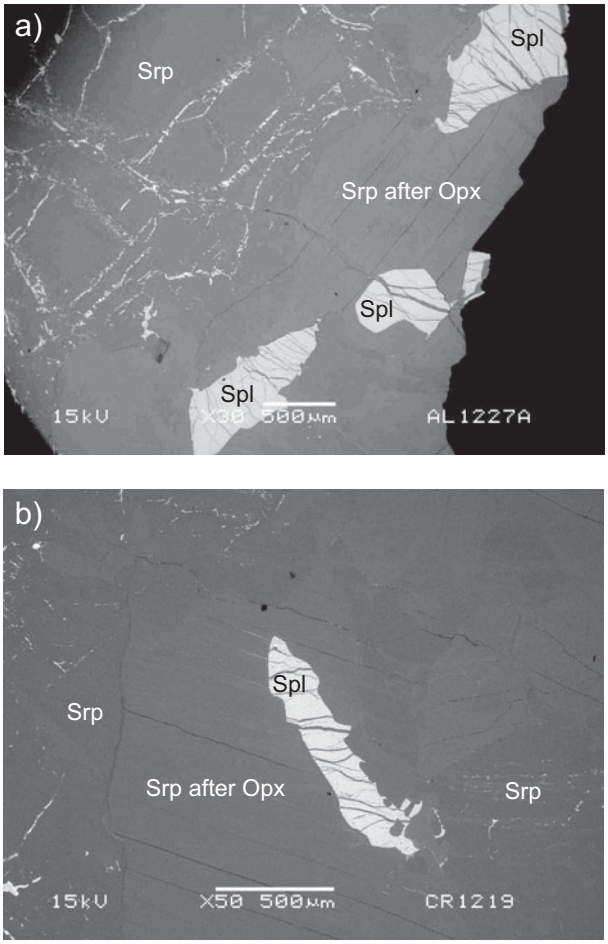

Figure 3. Back-scattered electron images of typical ETO Cr-spinel from (a) sample TD01003 and (b) TD01007. Spl – Cr-spinel; Srp – serpentine; Opx – orthopyroxene.

4. Methods

4.a. Electron probe micro-analyser (EPMA)

An electron probe micro-analyser (EPMA) was used to determine the major element composition of the Cr-spinel. For the analyses, the sample mounts were coated with carbon using a Quorum Technology Q150TE high vacuum carbon coater and loaded into the EPMA. For this study, a JEOL W-EPMA model JXA-8900-R with four wavelength dispersive spectrometers (WDS) at the Laboratory of Electron Probe Micro-Analyses, Institute of Earth Science, Academia Sinica was used. The electron beam was defocused at an interval of approximately 10 mm on an area of about 5 µm diameter with beam conditions of 15 kV and 12 nA. Back-scattered electron images were used to guide the analysis on target positions of minerals. The measurements were corrected by using standard minerals as follows: wollastonite for Si and Ca, rutile for Ti, corundum for Al, chrome oxide for Cr, haematite for Fe, tephroite for Mn, pyrope for Mg, nickel olivine for Ni, albite for Na, and adularia for K. Peak counting for each element and both upper and lower baselines were counted for 10 s and 5 s, respectively. Relative standard deviations (RSD) for all elements were less than 1 %.

4.b. Zircon U–Pb geochronology

Zircons were mechanically separated at the Yu-Neng Rock and Mineral Separation Co., Lanfang, Hubei province, China, using conventional heavy-liquid and magnetic separation techniques. Zircons were linearly mounted and polished to approximately half the mean grain thickness. A panchromatic cathodoluminescence (CL) imaging system (Gatan Mini-CL) attached to a scanning electron microscope (JOEL JSM-6360LV) was used to capture CL images of individual zircons to examine their internal structure. Laser ablation inductively coupled plasma mass spectrometer (LA-ICP-MS) U–Pb dating was carried out using an Agilent 7500cx quadrupole ICP-MS with a New Wave UP-213 laser ablation system at the Tectonics and Low-Temperature Heat Dating Laboratory, Department of Earth and Environmental Sciences, National Chung-Cheng University, Taiwan. The GJ-1 zircon was used as a standard for instrumental drift correction, which yielded an average ^{207}Pb–^{206}Pb age of 600 ± 5 Ma during experiments. The measured results of the zircon standard are within error of the reported age provided by thermal ionization mass spectrometry (TIMS) analyses by Jackson *et al.* (2004). The Plešovice zircon standard (337 ± 10 Ma) was used as a secondary standard for measurement quality control. Operating conditions and analytical procedures were the same as those reported by Chiu *et al.* (2009). Individual zircons were ablated using a beam diameter of 40 µm and frequency of 10 Hz.

4.c. X-ray fluorescence spectrometry (XRF)

Approximately 3 g of rock powder from each sample was heated to 100 °C for 3 hours to release ambient water from the sample and then heated to 900 °C for 6 hours to oxidize and release molecular water. The net weight change was recorded at each step and used to calculate the loss on ignition (LOI). A sample of 0.6 g of rock powder was thoroughly mixed with 6 g of Claisse® lithium borate with lithium bromide flux (49.75 % $Li_2B_4O_7$, 49.75 % $LiBO_2$ with 0.5 % LiBr). The mixed powder and flux was added to platinum (95 %) and gold (5 %) crucibles and fused at ~1200 °C to make a glass bead using a Claisse® M4 Fluxer. The analysis was conducted by a Panalytical Axios^{mAX} XRF spectrometer at the Department of Earth Sciences, National Taiwan Normal University. Standard reference materials analysed concurrent with the samples included AGV-2 (andesite), BIR-1a (Icelandic basalt) and DNC-1a (dolerite).

4.d. Inductively coupled plasma mass spectrometry (ICP-MS)

The bulk-rock trace element analyses were determined using a quadrupole inductively coupled plasma mass spectrometer (Q-ICP-MS, model Agilent 7500s) at the Geochemistry and Petrogenesis Lab, Department of Geosciences, National Taiwan University. The dissolved sample liquids used for ICP-MS were extracted

https://doi.org/10.1017/S0016756816000054 Published online by Cambridge University Press

Table 1. Average spinel compositions from the ETO peridotites

Sample No.	TD01001 8	s.d.	TD01002 22	s.d.	TD01003 20	s.d.	TD01004 17	s.d.	TD01007 26	s.d.	TD01008 35	s.d.	TD010013 24	s.d.
SiO_2 (wt %)	0.03	0.02	0.01	0.01	0.01	0.02	0.03	0.03	0.02	0.02	0.02	0.02	0.03	0.02
TiO_2	0.07	0.04	0.08	0.03	0.08	0.04	0.07	0.04	0.03	0.03	0.12	0.16	0.19	0.13
Al_2O_3	32.04	0.32	26.93	0.80	29.14	0.80	27.90	0.74	25.76	0.91	24.86	1.04	24.74	1.56
Cr_2O_3	35.34	1.00	41.39	0.80	38.95	1.29	39.38	1.11	41.93	1.32	43.85	1.09	43.35	1.05
FeOt	14.65	0.38	15.07	0.74	14.35	0.65	15.32	0.71	15.01	1.09	15.59	0.76	16.30	0.51
NiO	0.15	0.05	0.12	0.06	0.14	0.04	0.15	0.04	-	-	-	-	-	-
MnO	0.41	0.04	0.47	0.08	0.39	0.08	0.41	0.08	0.36	0.05	0.40	0.08	0.49	0.07
MgO	15.73	0.39	15.29	0.59	15.70	0.48	14.78	0.61	14.83	0.46	14.25	0.72	13.76	0.47
CaO	0.01	0.01	0.03	0.05	0.01	0.01	0.06	0.06	0.01	0.01	-	-	-	-
Sum	98.43	1.06	99.39	1.00	98.78	0.84	98.09	0.68	97.96	0.53	99.11	0.58	98.87	0.66
Fe_2O_3	2.79	0.64	3.12	0.47	2.78	0.59	2.79	0.55	2.76	0.94	2.13	0.63	2.21	0.61
FeO	12.14	0.58	12.26	0.72	11.85	0.84	12.81	1.10	12.53	0.77	13.68	1.16	14.31	0.67
Total	98.71	1.04	99.67	0.98	99.05	0.80	98.31	0.68	98.2	0.51	99.30	0.57	99.08	0.63
Si	0.001	0.001	-	-	-	-	0.001	0.001	0.001	0.001	0.001	0.001	0.001	0.001
Al^{vi}	1.111	0.011	0.948	0.020	1.019	0.027	0.992	0.027	0.924	0.031	0.890	0.034	0.891	0.046
Fe^{3+}	0.062	0.014	0.070	0.011	0.062	0.014	0.063	0.013	0.063	0.022	0.049	0.014	0.051	0.014
Ti	0.002	0.001	0.002	0.001	0.002	0.001	0.002	0.001	0.001	0.001	0.003	0.004	0.004	0.003
Cr	0.822	0.019	0.978	0.018	0.914	0.028	0.939	0.025	1.010	0.031	1.054	0.030	1.048	0.035
Fe^{2+}	0.299	0.015	0.306	0.020	0.294	0.021	0.323	0.028	0.319	0.020	0.348	0.031	0.366	0.019
Ni	0.003	0.001	0.003	0.001	0.003	0.001	0.004	0.001	-	-	-	-	-	-
Mn	0.010	0.001	0.012	0.002	0.010	0.002	0.011	0.002	0.009	0.001	0.010	0.002	0.013	0.002
Mg	0.690	0.015	0.681	0.020	0.695	0.021	0.665	0.027	0.673	0.020	0.646	0.030	0.627	0.018
Mg no.	69.8	1.5	69.0	2.0	70.3	2.1	67.3	2.8	67.8	2.0	65.0	3.1	63.2	1.9
Cr no.	42.5	0.7	50.8	0.9	47.3	1.4	48.6	1.3	52.2	1.5	54.2	1.6	54.1	2.1

No. – number of averaged analyses; s.d. – standard deviation; Mg no. = $(Mg/Mg + Fe^{2+}))^*100$; Cr no. = $(Cr/(Cr + Al))^*100$.

using the same procedure as the Sr and Nd isotopes. The standard reference materials measured for the trace elements were AGV-2, BIR-1 and DNC-1 with a precision better than 5 % (2σ) for most trace elements.

4.e. Thermal ionization mass spectrometry (TIMS)

The samples were dissolved using hydrofluoric acid (HF), nitric acid (HNO_3) and hydrochloric acid (HCl). The concentrates were loaded on a double rhenium filament. In this research, a Thermo Finnigan™ Mat GmbH MAT262Q thermal ionization mass spectrometer was used for Sr isotope analysis and a Thermo Scientific™ Triton Plus multicollector thermal ionization mass spectrometer was used for Nd isotope analysis, both at the Mass Spectrometer Lab, Institute of Earth Science, Academia Sinica.

5. Results

5.a. Spinel chemistry

The averaged Cr-spinel compositions are shown in Table 1 and the full results are listed in the online Supplementary Material Table S1 available at http://journals.cambridge.org/geo. The Cr_2O_3 content ranges from ~35 wt % for TD01001, to an intermediate range between 38 and 41 wt % for TD01002, TD01003 and TD01004 and a slightly higher concentration of 41 to 46 wt % for samples TD01007, TD01008 and TD01013. The mean aluminium content of all samples is ~26.5 wt %, while samples TD01001 and TD01003 have higher concentrations (32 and 29 wt %) and TD01008 and TD01013 have lower concentrations (25 wt %). The Cr^{3+} and Al^{vi} cations are used to calculate the Cr no. $((Cr^{3+}/(Cr^{3+} + Al^{vi}))^*100)$. The mean Cr no. of all samples is ~51.2. Sample TD01001 has the lowest average Cr no. of 43, whereas all other samples have values > 47. The highest average Cr no. is 54.2 from TD01008. The MgO content of the spinel is relatively constant at ~15 wt % but their overall range is from 12 wt % to 17 wt %. Total iron content for all samples is between 13 wt % and 17 wt %. The Mg no. (i.e. Mg no. $(((Mg^{2+}/(Mg^{2+} + Fe^{2+}))^*100)$) values are between 58 and 74. The concentrations of the remaining oxides (SiO_2, TiO_2, MnO, NiO, CaO, Na_2O and K_2O) are lower than 0.5 wt %.

5.b. Zircon U–Pb geochronology

The analysed zircons are ~100 to ~250 μm in diameter and have anhedral fragmented shapes. Some of the zircons have oscillatory zoning whereas others have complicated internal structures. Common lead was corrected using the common lead correction function of Andersen (2002, 2008). The U–Pb results are shown in Table 2. The Concordia diagram, constructed using Isoplot 3.0 (Ludwig, 2003), is shown in Figure 4 with 2σ error ellipses of the individual spot analyses. The weighted mean ^{206}Pb–^{238}U age is 14.1 ± 0.4 Ma on 20 individual zircon crystals and the MSWD (mean square weighted deviation) is 1.2 (Fig. 4). Owing to the young age of the zircons, the ^{207}Pb–^{235}U age has a larger uncertainty and thus has less significance.

5.c. Major and trace elemental chemistry

The serpentinized peridotites have 37.9 to 39.9 wt % SiO_2, 35.8 to 38.5 wt % MgO, 6.7 to 8.2 wt % Fe_2O_3

https://doi.org/10.1017/S0016756816000054 Published online by Cambridge University Press

Table 2. Zircon LA-ICP-MS geochronology results from the hornblende gabbro

Spot	$^{207}Pb/^{206}Pb$	± 1σ	$^{207}Pb/^{235}U$	± 1σ	$^{206}Pb/^{238}U$	± 1σ	Error correlation	$^{207}Pb–^{235}U$	$^{206}Pb–^{238}U$
14.1	0.0501	0.0043	0.0147	0.0018	0.0021	0.0001	0.3492	15 ± 2	13.7 ± 0.6
14.2	0.0541	0.0123	0.0165	0.0050	0.0022	0.0002	0.2852	17 ± 5	14 ± 1.0
14.3	0.0341	0.0059	0.0097	0.0021	0.0021	0.0001	0.2266	10 ± 2	13.3 ± 0.6
14.4	0.0460	0.0181	0.0128	0.0063	0.0020	0.0002	0.2316	13 ± 6	13 ± 1.0
14.5	0.0411	0.0191	0.0110	0.0058	0.0019	0.0001	0.1365	11 ± 6	12.5 ± 0.9
14.6	0.0513	0.0055	0.0150	0.0022	0.0021	0.0001	0.3216	15 ± 2	13.7 ± 0.6
14.7	0.0460	0.0045	0.0131	0.0018	0.0021	0.0001	0.3502	13 ± 2	13.3 ± 0.6
14.8	0.0465	0.0037	0.0148	0.0017	0.0023	0.0001	0.3460	15 ± 2	14.9 ± 0.6
14.9	0.0430	0.0020	0.0133	0.0010	0.0022	0.0001	0.4282	13.4 ± 1	14.4 ± 0.5
14.10	0.0397	0.0142	0.0131	0.0059	0.0024	0.0003	0.2318	13 ± 6	15 ± 2.0
14.11	0.0370	0.0128	0.0107	0.0045	0.0021	0.0002	0.2029	11 ± 5	14 ± 1.0
14.13	0.0460	0.0092	0.0155	0.0043	0.0025	0.0002	0.3125	16 ± 4	16 ± 1.0
14.14	0.0471	0.0246	0.0151	0.0093	0.0023	0.0003	0.1739	15 ± 9	15 ± 2.0
14.15	0.0463	0.0122	0.0144	0.0046	0.0023	0.0001	0.1952	15 ± 5	14.5 ± 0.9
14.16	0.0398	0.0055	0.0127	0.0024	0.0023	0.0001	0.3032	13 ± 2	14.9 ± 0.8
14.18	0.0411	0.0097	0.0124	0.0035	0.0022	0.0001	0.1937	12 ± 4	14 ± 0.8
14.19	0.0433	0.0070	0.0129	0.0027	0.0022	0.0001	0.2658	13 ± 3	13.9 ± 0.8
14.20	0.0363	0.0041	0.0123	0.0019	0.0025	0.0001	0.2964	12 ± 2	15.8 ± 0.7
14.21	0.0476	0.0054	0.0145	0.0023	0.0022	0.0001	0.3174	15 ± 2	14.3 ± 0.7
14.22	0.0447	0.0088	0.0132	0.0033	0.0021	0.0001	0.2454	13 ± 3	13.7 ± 0.8
Analyses not used									
14.12	0.0534	0.1196	0.0130	0.0330	0.0018	0.0006	0.1294	13 ± 33	14 ± 9.0
14.17	0.0462	0.0109	0.0143	0.0040	0.0023	0.0001	0.2286	14 ± 4	15 ± 2.0

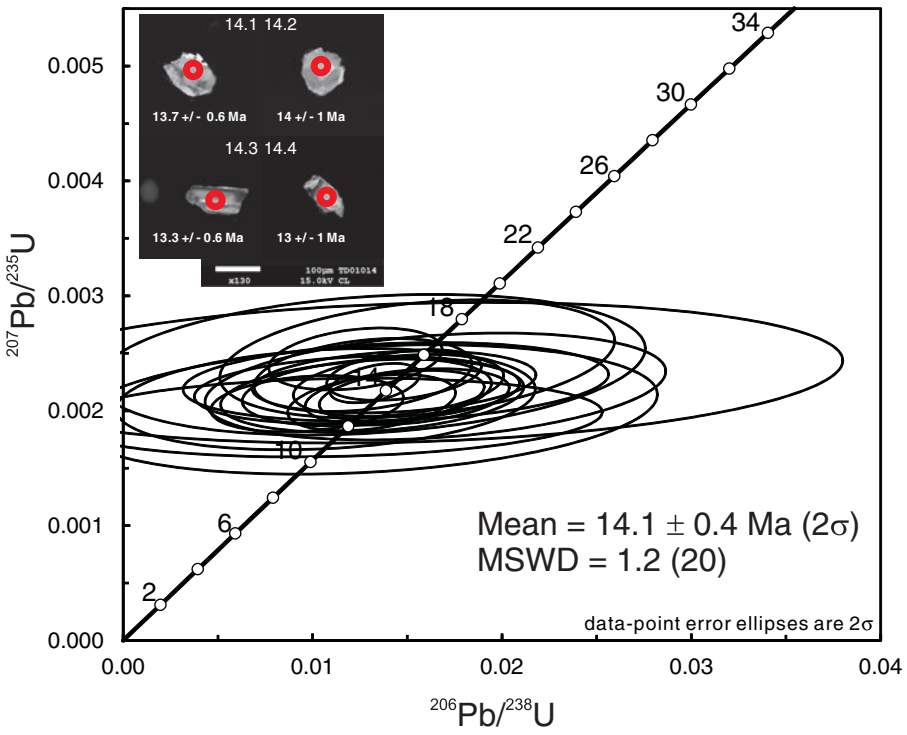

Figure 4. (Colour online) $^{207}Pb–^{235}U$ v. $^{206}Pb–^{238}U$ Concordia plot of the zircons from the ETO hornblende gabbro with cathodoluminescence images of typical zircons.

and < 1.0 wt % Al_2O. TiO_2, MnO, Na_2O, K_2O and P_2O_5 contents are close to the detection limit and/or not detected (Table 3). CaO content is more variable and is likely owing to the presence of secondary calcite veins in the rock. The Mg nos $(((Mg^{2+}/(Mg^{2+} + Fe^{2+}))*100))$ of the serpentinized peridotite samples are between 90 and 92.

The trace element concentrations of the serpentinized peridotites are quite low except for the transition metals (i.e. Sc, Ti, V, Cr, Mn, Co, Ni, Cu, Zn). Sr concentration in TD01002 (~219 ppm) is several times higher than in other samples (< 43 ppm). Sample TD01004 has a greater abundance of the high-field-strength and large-ion-lithophile elements (i.e. Ga, Rb, Y, Zr, Nb, Cs, Ba, Hf, Ta, Th) than the other samples. The rare earth element (REE) concentrations of all the serpentinized peridotites except TD01004 are low (< 0.1 ppm). TD01004 has much higher concentrations

https://doi.org/10.1017/S0016756816000054 Published online by Cambridge University Press

Table 3. Major and trace elemental data of the spinel peridotite and gabbro

Sample	TD01001	TD01002	TD01003	TD01004	TD01007	TD01008	TD010013	TD010014	TD01004(dup)	AGV-2 (m.v.)	AGV-2 (r.v.)	DNC-1 m.v.	DNC-1 r.v.	BIR-1 m.v.	BIR-1 m.v.
SiO_2 (wt %)	39.89	37.86	39.76	39.56	39.62	39.53	39.53	48.43	-	59.12	59.3	47.26	47.15	47.69	47.96
TiO_2	0.01	0.01	n.d.	0.01	n.d.	n.d.	0.01	2.59	-	1.02	1.05	0.49	0.48	0.96	0.96
Al_2O_3	0.68	0.67	0.62	0.89	0.59	0.55	0.72	12.13	-	17.29	16.91	18.28	18.34	15.43	15.5
Fe_2O_3t	7.45	6.74	7.28	7.42	7.97	8.22	8.05	18.09	-	6.68	6.69	9.77	9.97	11.17	11.3
MnO	0.07	0.07	0.07	0.08	0.09	0.09	0.09	0.15	-	-	-	0.15	0.15	0.17	0.175
MgO	37.52	35.80	37.94	36.56	38.47	37.96	38.13	5.89	-	1.73	1.79	10.10	10.13	9.59	9.70
CaO	0.73	3.42	0.66	1.65	0.05	0.07	0.05	8.08	-	5.10	5.20	11.24	11.49	13.22	13.3
Na_2O	n.d.	n.d.	n.d.	n.d.	n.d.	n.d.	n.d.	3.58	-	4.21	4.19	1.87	1.89	1.75	1.82
K_2O	0.01	n.d.	0.01	0.01	n.d.	0.01	n.d.	0.34	-	2.67	2.88	0.22	0.234	0.03	0.03
P_2O_5	n.d.	n.d.	n.d.	n.d.	n.d.	n.d.	n.d.	0.05	-	0.47	0.48	0.06	0.07	0.02	0.021
LOI	12.49	14.12	12.50	12.91	12.23	12.18	12.18	0.86	-	-	-	-	-	−0.28	-
Total	98.84	98.70	98.84	99.10	99.03	98.62	98.77	100.20	-	-	-	-	-	99.75	-
Mg no.	90.9	91.3	91.2	90.7	90.5	90.1	90.4	39.2	-	-	-	-	-	-	-
Sc (ppm)	7	7	8	8	10	9	9	59	19	12	13	32	31	44	-
V	33	29	25	30	37	35	36	860	30	118	120	154	148	318	-
Cr	2114	2446	1982	2259	2520	2292	2303	6	2641	19	17	285	270	384	-
Co	92	91	114	91	105	106	102	60	98	15	16	56	57	51	52
Ni	1875	1983	2196	1987	2017	2039	1976	111	2257	17	19	253	247	163	170
Cu	2	2	10	2	5	1	7	8	7	50	53	98	100	119	125
Zn	34	34	32	35	33	32	66	39	37	85	86	61	70	69	-
Ga	0.5	0.3	0.2	0.9	0.3	0.4	0.4	19	1.7	21	20	14	15	16	16
Rb	n.d.	n.d.	n.d.	1	n.d.	n.d.	n.d.	3	0.7	70	68.6	1	4.5	-	-
Sr	43	219	9	20	n.d.	n.d.	n.d.	119	21	657	658	147	144	112	110
Y	0.5	0.4	0.2	3.4	0.1	0.2	0.3	32	4	20	20	18	18.0	16	16
Zr	n.d.	n.d.	n.d.	3	n.d.	1	n.d.	38	3	229	230	35	38	14	-
Nb	n.d.	n.d.	n.d.	0.2	n.d.	n.d.	n.d.	0.8	0.5	14	15	1	3	-	-
Cs	n.d.	n.d.	n.d.	n.d.	n.d.	n.d.	n.d.	n.d.	n.d.	1	1.16	0.2	-	-	-
Ba	n.d.	n.d.	n.d.	n.d.	n.d.	n.d.	n.d.	7	6	1133	1140	101	118	12	-
La	n.d.	n.d.	0.100	0.300	n.d.	n.d.	n.d.	2	0.500	35.3	38	3.7	3.6	0.7	-
Ce	0.100	n.d.	n.d.	0.900	n.d.	0.100	n.d.	9	1.600	65.3	68	8.2	-	2.0	-
Pr	0.016	0.009	0.013	0.153	0.005	0.018	0.013	1.5	0.183	7.7	8.3	1.1	-	0.4	-
Nd	0.086	0.053	0.055	0.825	0.017	0.064	0.069	8.5	1.009	30.6	30	5.2	5.20	2.4	2.5
Sm	0.030	0.020	0.010	0.320	n.d.	0.020	0.030	3.1	0.320	5.6	5.7	1.5	-	1.1	1.1
Eu	0.005	0.004	0.001	0.048	n.d.	0.002	0.007	1.2	0.052	1.6	1.54	0.6	0.59	0.5	0.55
Gd	0.040	0.030	0.010	0.450	n.d.	0.020	0.040	4.3	0.430	4.4	4.69	2.1	2.0	1.9	2.0
Tb	0.009	0.005	0.003	0.087	0.001	0.003	0.007	0.8	0.099	0.6	0.64	0.4	-	0.4	-
Dy	0.080	0.040	0.020	0.610	0.010	0.020	0.050	5.4	0.680	3.4	3.6	2.7	3.0	2.5	-
Ho	0.017	0.011	0.005	0.137	0.002	0.005	0.011	1.2	0.156	0.6	0.71	0.6	0.62	0.6	-
Er	0.060	0.040	0.020	0.420	0.010	0.020	0.040	3.5	0.500	1.8	1.79	1.9	-	1.7	-
Tm	0.011	0.008	0.004	0.075	0.003	0.005	0.006	0.5	0.088	0.3	0.26	0.3	-	0.3	-
Yb	0.060	0.040	0.020	0.500	0.020	0.030	0.040	3.6	0.620	1.6	1.6	2.0	2.0	1.7	1.7
Lu	n.d.	n.d.	n.d.	0.062	n.d.	n.d.	n.d.	0.6	0.106	0.2	0.25	0.3	-	0.2	-
Hf	n.d.	n.d.	n.d.	0.120	n.d.	0.010	n.d.	11	1.010	4.9	5.08	0.9	-	0.5	0.6
Ta	0.005	0.001	0.004	0.030	0.003	0.009	0.001	n.d.	0.035	0.9	0.89	0.1	-	-	-
Th	n.d.	n.d.	n.d.	n.d.	n.d.	n.d.	n.d.	0.1	0.04	6.2	6.1	0.2	-	-	-
U	0.20	0.58	0.14	0.34	n.d.	n.d.	n.d.	n.d.	0.52	1.9	1.88	-	-	-	-

LOI – loss on ignition; Mg no. = $(Mg^{2+}/(Mg^{2+} + Fe^{2+}))^*100$; FeO – $0.8998^*Fe_2O_3t$; dup – duplicate; m.v. – measured value; r.v. – recommended value; n.d. – not detected.

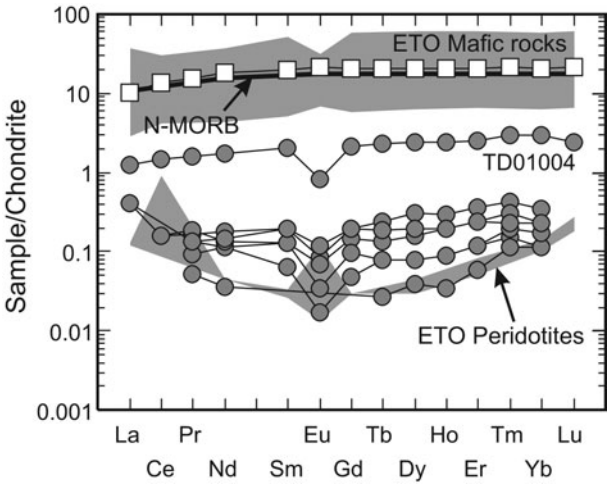

Figure 5. Chondrite-normalized REE plots of the spinel peridotites and hornblende gabbro. Normalized values are from Sun & McDonough (1989) and the range of ETO basalts and peridotites from Jahn (1986).

of REEs (~10 times) with an 'N-MORB-shaped' pattern whereas the other samples have a U-shaped pattern and negative Eu anomaly (Fig. 5). The REE concentrations are about 0.1 times C1 chondrite concentration, except TD01004, which has one to two times chondrite concentration.

The gabbro has 48.4 wt % SiO_2, 2.6 wt % TiO_2 and a Mg no. of 39 and classifies as normal mid-ocean ridge basalt (N-MORB) (Mullen, 1983). The transition metals are quite variable as V (~860 ppm), Ni (111 ppm) and Co (60 ppm) are relatively high whereas Cr (~6 ppm) and Cu (~8 ppm) are low. The chondrite-normalized REE pattern is light rare earth element (LREE) depleted (i.e. La/Yb_N = 0.4) and similar to N-MORB and other mafic rocks of the ETO (Fig. 5).

5.d. Sr–Nd isotope geochemistry

The $^{87}Sr/^{86}Sr$ isotope ratio of four samples (i.e. TD01001, TD01002, TD01003 and TD01004) ranges between 0.70883 and 0.70908 (Table 4). The initial $^{87}Sr/^{86}Sr$ values cannot be calculated (i.e. TD01001, TD01004, TD01003) owing to the extremely low Rb content (i.e. below detection limit) but given their likely age (i.e. ~14 Ma) the measured value will not be significantly different from the initial values (i.e. ± 0.00001). Sample TD01004 was the only one that had detectable quantities of Sm and Nd and produced a measured $^{143}Nd/^{144}Nd$ ratio of 0.513106. The initial ratio based on the age of the gabbro is 0.513083 and corresponds to an $\varepsilon_{Nd}(t)$ value of +9.1 using a $CHUR_{today}$ value of 0.512638 (Fig. 6). The gabbro has a measured $^{87}Sr/^{86}Sr$ isotope ratio of 0.70503 and corresponds to a $^{87}Sr/^{86}Sr_i$ value of 0.70501. The measured $^{143}Nd/^{144}Nd$ isotope ratio is 0.513226 with an $\varepsilon_{Nd}(t)$ value of +11.4 (Fig. 6).

Table 4. Sr–Nd isotopes of the peridotite and gabbro from the ETO

Sample	Rock	Rb (ppm)	Sr (ppm)	$^{87}Rb/^{86}Sr$	$^{87}Sr/^{86}Sr$	$\pm2\sigma_m$	I_{Sr}	Sm (ppm)	Nd (ppm)	$^{147}Sm/^{144}Nd$	$^{143}Nd/^{144}Nd$	$\pm2\sigma_m$	$\varepsilon_{Nd}(0)$	$\varepsilon_{Nd}(t)$	F (Sm/Nd)
TD01001	Peridotite	n.d.	43	-	0.708891	9	-	-	-	-	-	-	-	-	-
TD01002	Peridotite	n.d.	219	-	0.708833	7	-	-	-	-	-	-	-	-	-
TD01003	Peridotite	n.d.	9	-	0.709076	8	-	-	-	-	-	-	-	-	-
TD01004	Peridotite	0.72	21	0.099	0.709036	7	0.70901	0.32	0.825	0.2345	0.513106	6	+9.1	+9.1	0.19
TD010014	Gabbro	3	119	0.073	0.705030	7	0.70501	3.1	8.5	0.2205	0.513226	6	+11.5	+11.4	0.12

Rb, Sr, Sm and Nd concentrations were obtained by ICP-MS and the precisions are better than ±2 %. The results of isotopic measurements for Sr and Nd reference materials are NBS-987 (Sr) = 0.710248 ± 3 (2σm); JMC (Nd) = 0.511813 ± 10 (2σm). f(Sm/Nd) is defined as $((^{147}Sm/^{144}Nd)/0.1967-1)$. $\varepsilon_{Nd}(t)$ is calculated using an approximate equation of $\varepsilon_{Nd}(t) = \varepsilon_{Nd}(0) - Q^*f^*T$, in which Q = 25.1 Ga^{-1}; f = f(Sm/Nd); T age = 0.015 Ga; $T_{DM} - 1 = (1/\lambda)^*\ln(1 + ((^{143}Nd/^{144}Nd)_m - 0.51315)/((^{147}Sm/^{144}Nd)_m - 0.2137))$; λ = 0.00654 Ga^{-1}.

https://doi.org/10.1017/S0016756816000054 Published online by Cambridge University Press

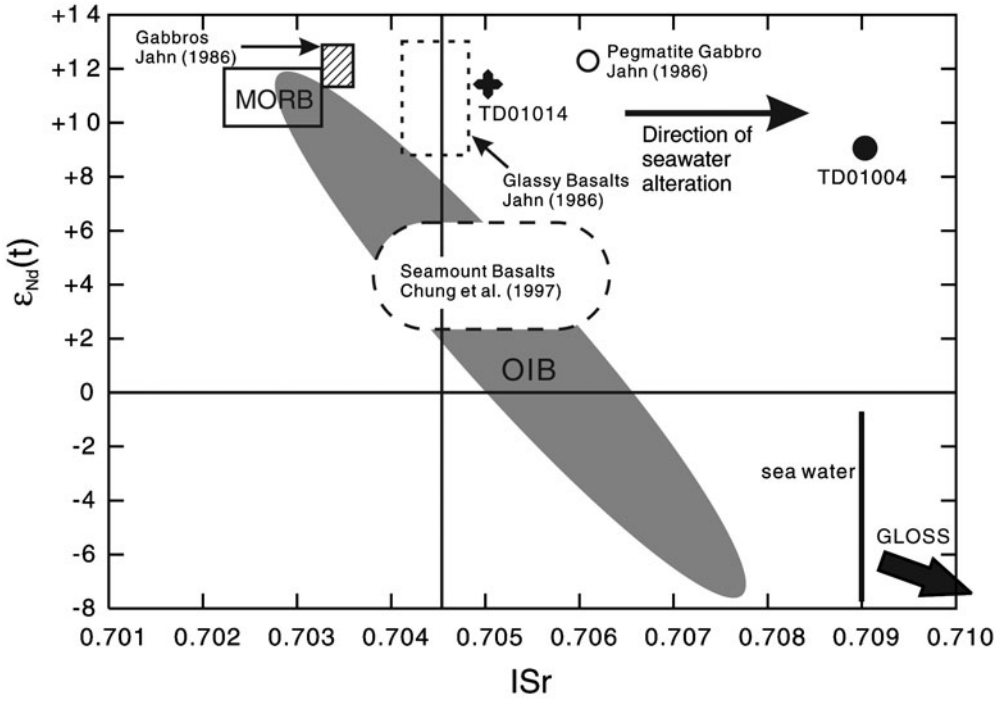

Figure 6. Initial Sr and Nd isotopes of the ETO rocks including the peridotite and gabbro from this study. Previously reported data from Jahn (1986) and Chung *et al.* (1997). The Sr isotopes were likely affected by seawater alteration.

6. Discussion

6.a. Age of the East Taiwan Ophiolite

Huang, Chen & Chi (1979) first attempted to determine the age of the ETO by identifying foraminifera species *Sphenolithus heteromorphus* and *Calcidiscus macintyrei* within red shales from nanofossil zone NN5, which constrains the deposition age to lower and middle Miocene. Jahn (1986) reported the first radioisotopic ages for two types of basaltic rock (i.e. glass and crystalline), plagiogranite and gabbro using the K–Ar method. The results produced four different ages: 33 ± 5 Ma (plagiogranite), 14.6 ± 0.4 Ma (basaltic glass), 11 ± 4 Ma (gabbro) and 8.1 ± 0.9 Ma (crystalline basalt). Consequently, Jahn (1986) interpreted the likely age of the ETO to be 14.6 ± 0.4 Ma based on mutual consistency with the palaeontological interpretations of Huang, Chen & Chi (1979). Recently, U–Pb age dates were reported by W. Y. Shao (unpub. Ph.D. thesis, National Taiwan Univ., 2015) on gabbro and diorite from the north branch of the Chiawu creek. The concordant ages of the gabbros are ~17.5 Ma (i.e. 17.5 ± 0.2 Ma and 17.4 ± 0.2 Ma) whereas the diorites are 14.3 ± 0.5 Ma and plagiogranites are 14.1 ± 0.2 Ma.

The mean zircon U–Pb date from the hornblende gabbro (i.e. 14.1 ± 0.4 Ma) in this study is in agreement with the previous suggested age range: the K–Ar age of the basaltic glass (Jahn, 1986), the U–Pb zircon age of the diorite group (W. Y. Shao, unpub. Ph.D. thesis, National Taiwan Univ., 2015) and the interpreted age of the syn-ETO magmatism red shale layers (Huang, Chen & Chi, 1979). Therefore, in light of our new radioisotopic ages, the ETO is probably no older than middle Miocene. This implies that the magmatism and sea-floor spreading within the South China Sea was still active for at least ~1.5 million years after the inferred terminal age (i.e. ~15.5 Ma).

6.b. Tectonic setting of the East Taiwan Ophiolite

The rock sequence of the ETO is described in previous studies but all units that are common to the idealized stratigraphy of an ophiolite are present (Fig. 2) (Anonymous, 1972; Liou *et al.* 1977; Liou & Ernst, 1979; Suppe, Liou & Ernst, 1981; Chung & Sun, 1992; Dilek, 2003). The red shale layers between the intrusive rocks and the extrusive rocks indicate that they were exposed under the carbonate compensation depth (CCD) for a period of time, perhaps a deep-ocean setting at great distance from land (Chung & Sun, 1992).

Bonatti & Michael (1989) demonstrated that whole-rock Mg no. and Al content can be effective in distinguishing peridotites derived at ridge settings, passive margin settings, pre-oceanic rift and oceanic trench settings because they are relatively immobile during serpentinization. Moreover the Cr no. and Mg no. of spinel from mantle peridotite are useful for interpreting the tectonic setting because they are indicators of the degree of depletion within the mantle source and also they are relatively unaffected by hydrothermal conditions commonly experienced by oceanic peridotites (Dick & Bullen, 1984; Bonatti & Michael, 1989; Arai, 1994). Figures 7 and 8 show that all serpentinized peridotites from the ETO have Mg nos (i.e. 90 to 93), bulk-rock

https://doi.org/10.1017/S0016756816000054 Published online by Cambridge University Press

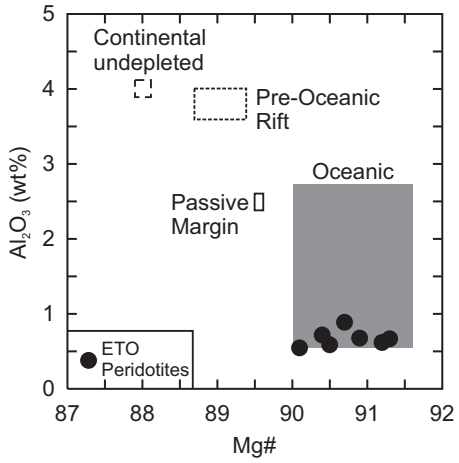

Figure 7. Range of whole-rock Mg nos and Al_2O_3 (wt%) of peridotites from different tectonic settings (based on Bonatti & Michael, 1989).

aluminium content and spinel compositions consistent with peridotites from an ocean ridge setting.

The REE patterns of the ETO serpentinized peridotites suggest there are at least two different rock types: (1) the U-shaped patterned rocks and (2) the 'N-MORB'-shaped patterned rock (Fig. 5). The relatively enriched 'N-MORB'-shaped pattern for sample TD01004 is similar to spinel lherzolites from the Pyrenees whereas the flat and U-shaped patterns resemble harzburgites from the Pyrenees, but the range of compositions are typical of orogenic peridotite massifs and ophiolites in general (Prinzhofer & Allegre, 1985; McDonough & Frey, 1989; Bodinier & Godard, 2003). The U-shaped patterns are probably not related to metasomatism by continental derived fluids (c.f. Gruau *et al.* 1998) because: (1) continental crust was not located near the easternmost South China Sea ridge and (2) the ETO basaltic rocks show evidence of seawater alteration rather than meteoric water (Liou & Ernst, 1979; Liou, 1979; Jahn, 1986). Element mobility is unlikely to be the reason why there are two types of serpentinized peridotites because REEs tend to be immobile but also the patterns would be expected to be random or at least unique to the ETO rather than appearing similar to peridotites from other ophiolites or orogenic massifs (c.f. Greenough, Fryer & Robinson, 1990; Bodinier & Godard, 2003; Pearce, 2014). The depletion of Eu in TD01004 could be due to seawater alteration as Eu^{2+} can substitute for Ca^{2+} in silicate mineral systems but the remaining elements do not show anomalous patterns.

The depleted $\varepsilon_{Nd}(t)$ values of the serpentinized peridotite and basaltic rocks (i.e. +9 to +11), the depleted LREE pattern (i.e. $La/Yb_N = 0.4$) and N-MORB composition of the mafic rocks, and the spinel compositions of the serpentinized peridotites are consistent with a depleted mantle source and rocks found at a seafloor ridge setting. Therefore, the initial interpretations of Liou *et al.* (1977) and Jahn (1986) are likely correct and that the ETO was a mid-ocean ridge setting, but it is still uncertain if it was a slow-spreading ridge as proposed by Chung & Sun (1992).

6.c. Preservation of the ETO

There are a number of mid-ocean ridge type ophiolites in the geological record (i.e. Macquarie Island and Masirah), but the majority of ophiolites appear to be subduction-related, probably owing to their greater likelihood of preservation (Pearce, Lippard & Roberts, 1984; Stern & Bloomer, 1992; Peters & Mercolli, 1998; Kamenetsky *et al.* 2000; Milsom, 2003; Pearce, 2003; Whattam & Stern, 2011; Dilek & Furnes, 2011, 2014). Nearly all of the Western Pacific and Cordilleran belt group of ophiolites are interpreted as subduction-related (i.e. suprasubduction zone or volcanic-arc); thus, the ETO may be a unique example of a subduction-unrelated ophiolite. In some cases arc rocks are not immediately discovered within specific ophiolite complexes such as the Semail ophiolite (Whattam & Stern, 2011; Dilek & Furnes, 2011, 2014). Consequently the ETO could represent a suprasubduction zone ophiolite in which the 'arc-like' rocks (e.g. calc-alkaline affinity or boninite) have yet to be discovered, but that seems unlikely considering the current state of knowledge on the basaltic rocks and the results presented in this study (Jahn, 1986; Chung & Sun, 1992). Therefore, the main issue regarding the ETO is the mechanism of preservation. In other words, how was the ridge of the South China Sea accreted to the margin of Eurasia?

The ETO is highly dismembered and within a sedimentary mélange that formed prior to the collision of the Luzon arc with the Eurasian continental margin (Liou *et al.* 1977). Before accretion and collision the eastern margin of the Philippine Sea plate Luzon arc was translated hundreds of kilometres northwards as the northern margin was subducted beneath the Ryukyu arc (Teng, 1990). It is very likely that as northward left-lateral translation occurred, the easternmost spreading centre of the Sea China Sea was 'guillotined' or sheared off and blocks/debris were transferred to the Philippine Sea plate that subsequently accreted to Taiwan as the Luzon arc collided with the Eurasian margin (Fig. 9). In most cases ocean ridges are less likely to be preserved because they are subducted but in the case of the ETO, the tectonic dynamics (i.e. translation and accretion) were probably suitable for preservation (Wakabayashi & Dilek, 2003).

6.d. Implications for the South China Sea

The tectonic development of the South China Sea is a highly debated issue (Barckhausen *et al.* 2014, 2015; Li *et al.* 2014; Chang *et al.* 2015). The duration of spreading, in particular, is one of a number of issues that has yet to be fully resolved (Table 5). Originally Taylor & Hayes (1980, 1983) proposed a magnetic anomaly chronology for the South China Sea basin which is still widely accepted (11 to 5d, Taylor & Hayes, 1980, 1983; revised to 11 to 5c, Briais, Patriat & Tapponnier, 1993). They identified an E–W-oriented spreading centre between the Macclesfield Bank and Reed Bank

https://doi.org/10.1017/S0016756816000054 Published online by Cambridge University Press

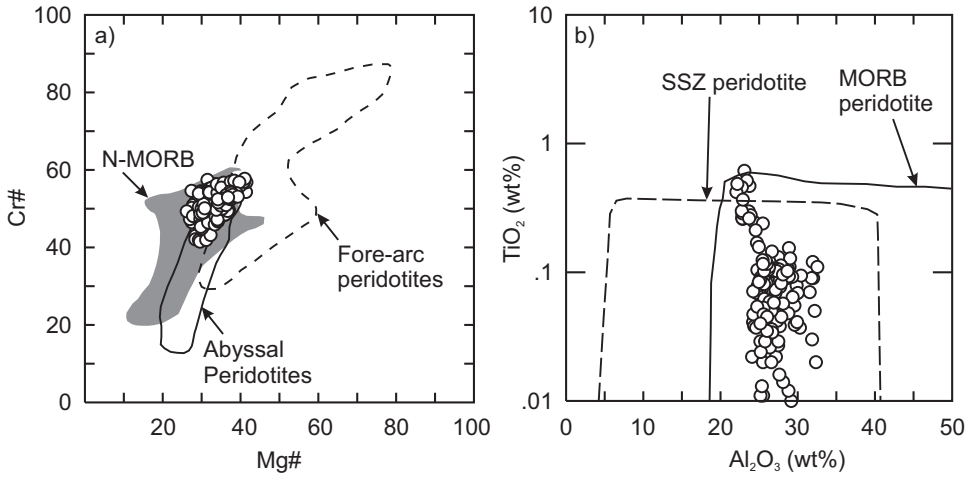

Figure 8. Tectonic discrimination diagrams of Dick & Bullen (1984) for Cr-spinel from peridotites using the (a) Cr no. and Mg no. and (b) Al_2O_3 and TiO_2 (wt %) from the ETO.

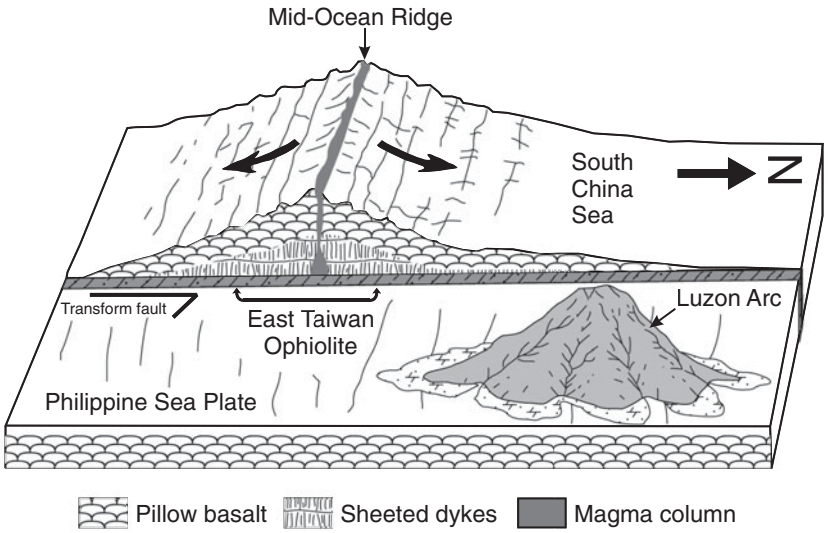

Figure 9. Conceptual tectonic model of the preservation of the ETO. The northward subduction of the Philippine Sea plate beneath the Ryukyu arc initiates translation between the Philippine Sea plate and the South China Sea. Blocks and debris from the ridge section of the South China Sea are deposited on the Philippine Sea plate and/or shear off as the northward migrating Luzon arc passes the easternmost ridge section. The blocks and debris (i.e. ETO) of the ridge along with the Luzon arc volcanoes are accreted to the Eurasian margin during late Pliocene time.

(Fig. 9), where the symmetric anomalies 5d through 6c have been modelled to the north and south. Beyond the Macclesfield Bank and close to South China were anomalies 7 to 11. The spreading ridge has a conjunction from a NW–SE direction to an E–W direction, and it is interpreted to be a result of a ridge jump that occurred at anomaly 7 (~24.8 Ma to 25 Ma) (Briais, Patriat & Tapponnier, 1993; Barckhausen & Roeser, 2004; Barckhausen *et al.* 2014; Li *et al.* 2014).

The duration of tectonomagmatic activity of the South China Sea is generally accepted to be a ~16.5 million-year interval from 32 Ma to 15.5 Ma (Taylor & Hayes, 1980, 1983; Briais, Patriat & Tapponnier, 1993); however, Barckhausen & Roeser (2004) suggested the South China Sea was active only for 11.5 Ma from 32 Ma to 20.5 Ma. Barckhausen *et al.* (2014) supported the short duration interpretation by proposing a new spreading rate for the South China Sea before and after the ridge jump, suggesting a 56 mm yr^{-1} rate in the early stages increasing to 72 mm yr^{-1} after the ridge jump in the central and NE sub-basin, and increasing to 80 mm yr^{-1} in the SW sub-basin. Li *et al.* (2014) suggested that the age of spreading is 33 Ma to 15 Ma and that the ridge jump occurred at ~23.6 Ma, based on new deep-tow magnetic anomalies and an IODP Expedition 349 core. Li *et al.* (2014) disagreed with the spreading rate proposed by Barckhausen *et al.* (2014) as they pointed out the spreading rate decreased from ~50 mm yr^{-1} to ~35 mm yr^{-1} during the later stages of spreading instead of increasing to 72 mm yr^{-1} after the ridge jump. Chang *et al.* (2015) also commented that Barckhausen & Roeser (2004) and Barckhausen *et al.* (2014) had neglected the radioisotopic age of Jahn (1986) and nanofossil assemblage from the ETO

https://doi.org/10.1017/S0016756816000054 Published online by Cambridge University Press

Table 5. Age estimates of the South China Sea (SCS) basin from previous studies

Authors	Ages (Ma)	Study area	Data used
Taylor & Hayes (1980, 1983)	32–17	East sub-basin	Magnetic anomaly
Briais, Patriat & Tapponnier (1993)	32–15.5	Central SCS basin	Magnetic anomaly
Barckhausen & Roeser (2004); Barckhausen *et al*. (2014)	31–20.5	Central SCS basin	Magnetic anomaly
Hsu *et al*. (2004)	37–15	Central SCS basin & NE SCS sub-basin	Magnetic anomaly
Li *et al*. (2014)	33–15	SW SCS sub-basin	Magnetic anomaly
	33–16	NE SCS sub-basin	

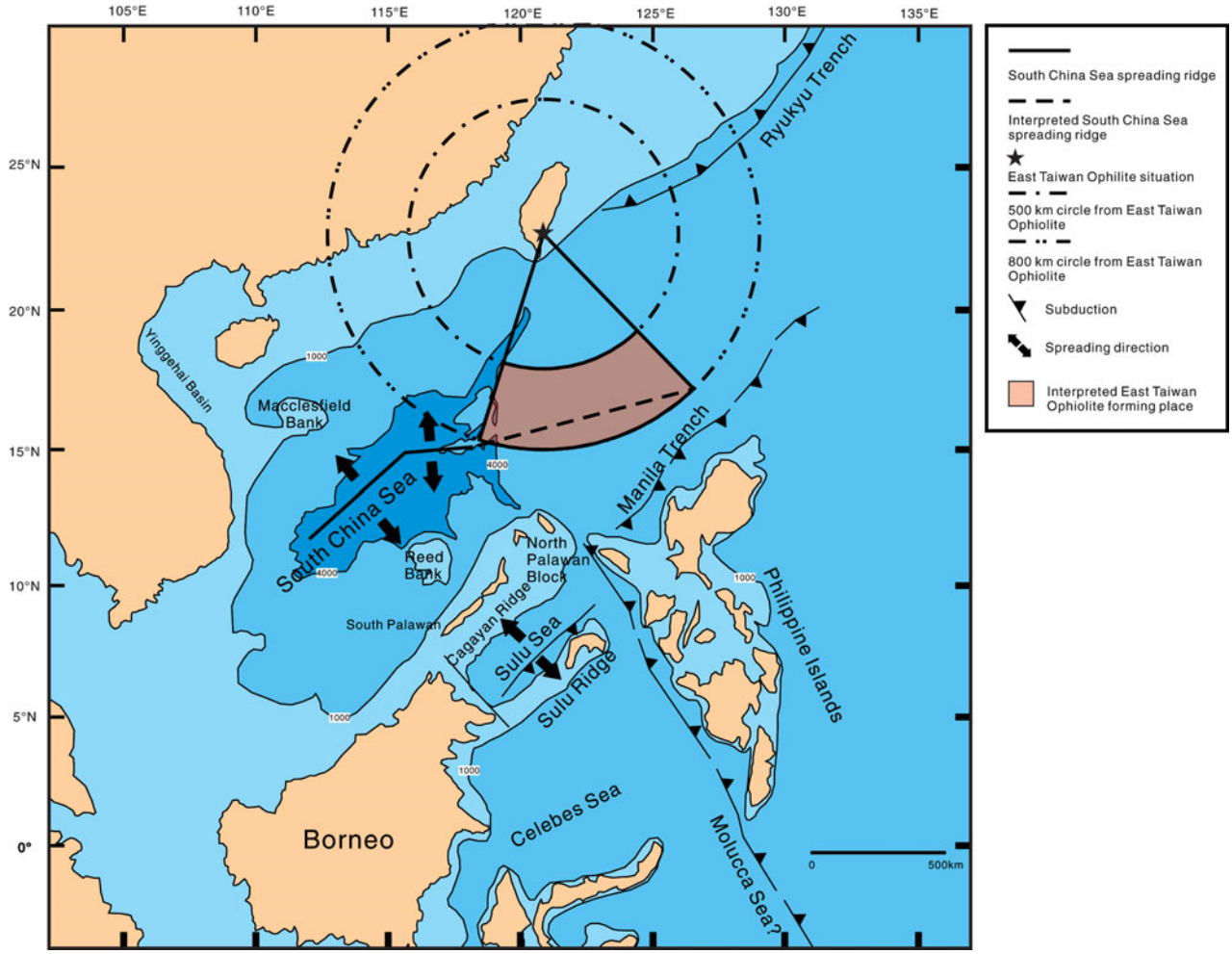

Figure 10. Possible palaeographic reconstruction of the South China Sea and likely location of the ETO at ~15 Ma (revised from Lee & Lawver, 1995).

(Huang, Chen & Chi, 1979) and advocated that the slow-spreading ridge is a more plausible model for the South China Sea.

If the ETO is a remnant of the South China Sea, the new age result in this study and by W. Y. Shao (unpub. Ph.D. thesis, National Taiwan Univ., 2015) suggests that magmatism and thus sea-floor spreading of the South China Sea lasted until middle Miocene time (i.e. ~14 Ma) and is ~1.5 million years younger than the accepted age. Jahn (1986) suggested the ETO had a life span of < 10 Ma based on a spreading rate of ~10 cm yr^{-1} indicating that it travelled a maximum distance of 1000 km. However, the ~10 cm yr^{-1} rate may be too fast and the ~1000 km distance may be too large, but a rate of 5–8 cm yr^{-1} and maximum distance of 500 km to 800 km may be suitable (Ben-Avraham & Uyeda, 1973; Hall *et al.* 1995; Teng & Lin, 2004). From previous studies, the collision of the Luzon arc with the Eurasian continental margin occurred at ~4–5 Ma (Jahn, 1986; Teng, 1987, 1990, 2007). Thus, the duration of the displacement of the ETO from the ridge to its current location would take ~10 million years (i.e. ~14.3 Ma to ~4.5 Ma). Based on a 5–8 cm yr^{-1} moving rate and 10 million-year duration, the possible displacement distance is between 500 km and 800 km, which are drawn as dashed circles in Figure 10. Figure 10 shows the estimated part of the South China Sea spreading ridge (dashed line) that was consumed beneath the Manila Trench and the orange zone is the general area of spreading and the likely

https://doi.org/10.1017/S0016756816000054 Published online by Cambridge University Press

original location of the ETO as it propagated eastwards (Lee & Lawver, 1995; Zhu *et al.* 2004).

7. Conclusions

The new whole-rock major and trace elemental and isotopic geochemistry, mineral chemistry and zircon U–Pb age data presented here and from previous studies suggest that the ETO has characteristics that are typically found at spreading ridges of oceanic crust. The Cr no. of spinel and bulk-rock Al and Mg contents are consistent with the oceanic ridge setting. The depleted Nd isotopes of the gabbro and serpentinized peridotite and the N-MORB-like REE pattern of the ETO mafic rocks are consistent with a mid-ocean ridge environment. The middle Miocene zircon U–Pb age of the ETO gabbro is ~1.5 Ma younger than the last magnetic anomaly of the South China Sea (i.e. 5c) and suggests that magmatism and sea-floor spreading were still occurring. Moreover, the possible original location of the ETO is between 500 and 800 km south of Taiwan and within an area of ~100 000 km^2.

Acknowledgements. We thank Scott Whattam, an anonymous reviewer and Phil Leat for important editorial comments. We also thank George Ma, Yoshiyuki Iizuka, Kuo-Lung Wang, Typhoon Lee, Sun-Lin Chung and Yuan-Hsi Lee for their assistance with field and laboratory work. JGS thanks the Ministry of Science and Technology (Taiwan) for financial support through grant 102-2628-M-003-001-MY4.

Supplementary material

To view supplementary material for this article, please visit http://dx.doi.org/10.1017/S0016756816000054.

References

ANDERSEN, T. 2002. Correction of common lead in U–Pb analyses that do not report ^{204}Pb. *Chemical Geology* **192**, 59–79.

ANDERSEN, T. 2008. ComPbCorr-Software for common lead correction of U-Th-Pb analyses that do not report ^{204}Pb. In *Laser Ablation-ICP-MS in the Earth Sciences: Current Practices and Outstanding Issues* (ed. P. Sylvester), pp. 312–4. Mineralogical Association of Canada Short Course Series 40.

Anonymous. 1972. Penrose Field Conference on Ophiolites. *Geotimes* **17**, 24–5.

ARAI, S. 1992. Chemistry of chromian spinel in volcanic rocks as a potential guide to magma chemistry. *Mineralogical Magazine* **56**, 173–84.

ARAI, S. 1994. Characterization of spinel peridotites by olivine-spinel compositional relationships: review and interpretation. *Chemical Geology* **113**, 191–204.

ARFAI, J., FRANKE, D., GAEDICKE, C., LUTZ, R., SCHNABEL, M., LADAGE, S., BERGLAR, K., AURELIO, M., MONTANO, J. & PELLEJERA, N. 2011. Geological evolution of the West Luzon basin (South China Sea, Philippines). *Marine Geophysical Research* **32**, 349–62.

BARCKHAUSEN, U., ENGELS, M., FRANKE, D., LADAGE, S. & PUBELLIER, M. 2014. Evolution of the South China Sea: revised ages for breakup and seafloor spreading. *Marine and Petroleum Geology* **58**, 599–611.

BARCKHAUSEN, U., ENGELS, M., FRANKE, D., LADAGE, S. & PUBELLIER, M. 2015. Reply to Chang *et al.* 2014. Evolution of the South China Sea: revised ages for breakup and seafloor spreading. *Marine and Petroleum Geology* **59**, 679–81.

BARCKHAUSEN, U. & ROESER, H. A. 2004. Seafloor spreading anomalies in the South China Sea revisited. In *Continent-Ocean Interactions Within East Asian Marginal Seas* (eds P. Clift, W. Kuhnt, P. Wang, & D. E. Hayes), pp. 121–5. American Geophysical Union, Geophysical Monograph vol. 149. Washington, DC, USA.

BEN-AVRAHAM, Z. & UYEDA, S. 1973. The evolution of the China Basin and the Mesozoic paleogeography of Borneo. *Earth and Planetary Science Letters* **18**, 365–76.

BODINIER, J. L. & GODARD, M. 2003. Orogenic, ophiolitic, and abyssal peridotites. In *Treatise on Geochemistry* (eds H. D. Holland & K. K. Turekian), pp. 103–70. Amsterdam: Elsevier.

BONATTI, E. & MICHAEL, P. J. 1989. Mantle peridotite from continental rifts to ocean basins to subduction zones. *Earth and Planetary Science Letters* **91**, 297–311.

BOWIN, C., LU, R. S., LEE, C. S. & SCHOUTEN, H. 1978. Plate convergence and accretion in the Taiwan-Luzon region. *American Association of Petroleum Geologists Bulletin* **62**, 1645–72.

BRIAIS, A., PATRIAT, P. & TAPPONNIER, P. 1993. Updated interpretation of magnetic anomalies and seafloor spreading stages in the South China Sea: implications for the Tertiary tectonics of Southeast Asia. *Journal of Geophysical Research* **98**, 6299–328.

CHAI, B. H. T. 1972. Structure and tectonic evolution of Taiwan. *American Journal of Science* **272**, 389–422.

CHANG, J. H., LEE, T. Y., HSU, H. H. & LIU, C. S. 2015. Comment on Barckhausen *et al.* 2014 – Evolution of the South China Sea: revised ages for breakup and seafloor spreading. *Marine and Petroleum Geology* **59**, 676–8.

CHEN, W. S., HUANG, M. T. & LIU, T. K. 1991. Neotectonic significance of the Chimei Fault in the Coastal Range, eastern Taiwan. *Proceedings of the Geological Society of China* **34**, 43–56.

CHIU, H.-Y., CHUNG, S.-L., WU, F.-Y., LIU, D., LIANG, Y.-H., LIN, I. J., IIZUKA, Y., XIE, L.-W., WANG, Y. & CHU, M.-F. 2009. Zircon U–Pb and Hf isotopic constraints from eastern Transhimalayan batholiths on the precollisional magmatic and tectonic evolution in southern Tibet. *Tectonophysics* **477**, 3–19.

CHUNG, S. L., CHENG, H., JAHN, B. M., O'REILLY, S. Y. & ZHU, B. 1997. Major and trace element, and Sr–Nd isotope constraints on the origin of Paleogene volcanism in South China prior to the South China Sea opening. *Lithos* **40**, 203–20.

CHUNG, S. L. & SUN, S. S. 1992. A new genetic model for the East Taiwan Ophiolite and its implications for Dupal domains in the Northern Hemisphere. *Earth and Planetary Science Letters* **109**, 133–45.

DICK, H. J. B. & BULLEN, T. 1984. Chromian spinel as a petrogenetic indicator in abyssal and alpine-type peridotites and spatially associated lavas. *Contributions to Mineralogy and Petrology* **86**, 54–76.

DILEK, Y. 2003. Ophiolite concept and its evolution. In *Ophiolite Concept and the Evolution of Geological Thought* (eds Y. Dilek & S. Newcomb), pp. 1–16. Geological Society of America, Special Paper no. 373.

DILEK, Y. & FURNES, H. 2011. Ophiolite genesis and global tectonics: geochemical and tectonic fingerprinting of ancient oceanic lithosphere. *Geological Society of America Bulletin* **123**, 387–411.

DILEK, Y. & FURNES, H. 2014. Ophiolites and their origins. *Elements* **10**, 93–100.

FLOWER, M., TAMAKI, K. & HOANG, N. 1998. Mantle extrusion: a model for dispersed volcanism and DUPAL-like asthenosphere in East Asia and the western Pacific. In *Mantle Dynamics and Plate Interactions in East Asia* (eds M. F. J. Flower, S. L Chung, C. H. Lo & T. Y. Lee), pp. 67–88. American Geophysical Union, Geodynamic Series 27.

FRANKE, D., SAVVA, D., PUBELLIER, M., STEUER, S., MOULY, B., AUXIETRE, J.-L., MERESSE, F. & CHARMOT-ROOKE, N. 2014. The final rifting evolution in the South China Sea. *Marine and Petroleum Geology* **58**, 704–20.

GREENOUGH, J. D., FRYER, B. J. & ROBINSON, P. T. 1990. Geochemical effects of alteration on mafic rocks from Indian Ocean site 706. In *Proceedings of the Ocean Drilling Program, Scientific Results, vol. 115* (eds R. A. Duncan, J. Backman & L. C. Peterson, P. A. Baker, A. N. Baxter, A. Boersma, J. L. Cullen, A. W. Droxler, M. R. Fisk, J. D. Greenough, R. B. Hargraves, P. Hempel, M. A. Hobart, M. T. Hurley, D. A. Johnson, A. H. Macdonald, N. Mikkelsen, H. Okada, D. Rio, S. G. Robinson, D. Schneider, P. K. Swart, Y. Tatsumi, D. Vandamme, G. Vilks & E. Vincent), pp. 85–92. College Station, Texas.

GRUAU, G., BERNARD-GRIFFITHS, J. & LECUYER, C. 1998. The origin of U-Shaped rare earth patterns in ophiolite peridotites: assessing the role of secondary alteration and melt/rock reaction. *Geochimica et Cosmochimica Acta* **62**, 3545–60.

HALL, R., ALI, J. R., ANDERSON, C. D. & BAKER, S. J. 1995. Origin and motion history of the Philippine Sea Plate. *Tectonophysics* **251**, 229–50.

HEBERT, R., HOUT, F., WANG, C. S. & LIU, Z. F. 2003. Yarlung Zanboo ophiolites (southern Tibet) revisited: geodynamic implications from the mineral record. In *Ophiolites in Earth History* (eds Y. Dilek & P. T. Robinson), pp. 165–90. Geological Society of London, Special Publication no. 218.

HSU, S. K., YEH, Y. C., DOO, W. B. & TSAI, C. H. 2004. New bathymetry and magnetic lineations identifications in the northernmost South China Sea and their tectonic implications. *Marine Geophysical Researchers* **25**, 29–44.

HUANG, T. C., CHEN, M. P. & CHI, W. R. 1979. Calcareous nanofossils from the red shale of the ophiolite-mélange complex, eastern Taiwan. *Memoir of the Geological Society of China* **3**, 131–8.

HUANG, C. Y., YUAN, P. B. & TSAO, S. J. 2006, Temporal and spatial records of active arc-continent collision in Taiwan: a synthesis. *Geological Society of America Bulletin* **118**, 274–88.

JACKSON, S. E., PEARSON, N. J., GRIFFIN, W. L. & BELOUSOVA, E. A. 2004. The application of laser ablation-inductively coupled plasma-mass spectrometry to in situ U–Pb zircon geochronology. *Chemical Geology* **211**, 47–69.

JAHN, B. M. 1986. Mid-ocean ridge or marginal basin origin of the East Taiwan Ophiolite: chemical and isotopic evidence. *Contributions to Mineralogy and Petrology* **92**, 194–206.

KAMENETSKY, V. S., CRAWFORD, A. J. & MEFFRE, S. 2001. Factors controlling chemistry of magmatic spinel: an empirical study of associated olivine, Cr-spinel and melt inclusions from primitive rocks. *Journal of Petrology* **42**, 655–71.

KAMENETSKY, V. S., EVERARD, J. L., CRAWFORD, A. J., VARNE, R., EGGINS, S. M. & LANYON, R. 2000. Enriched end-member of primitive MORB melts: petrology and geochemistry of glass from Macquarie Island (SW Pacific). *Journal of Petrology* **41**, 411–30.

KAO, H., SHEN, S. J. & MA, K. F. 1998. Transition from oblique subduction to collision: earthquakes in the southernmost Ryukyu Arc – Taiwan region. *Journal of Geophysical Research* **103**, 7211–29.

LEE, T. Y. & LAWVER, L. A. 1995. Cenozoic plate reconstruction of Southeast Asia, *Tectonophysics* **251**, 85–138.

LEE, C. T. & WANG, Y. 1987. Paleostress change due to the Pliocene–Quaternary arc-continent collision. *Memoir of the Geological Society of China* **9**, 63–86.

LI, C. F., XU, X., LIN, J., SUN, Z., ZHU, J., YAO, Y., ZHAO, X., LIU, Q., KULHANEK, D. K., WANG, J., SONG, T., ZHAO, J., QIU, N., GUAN, Y., ZHOU, Z., WILLIAMS, T., BAO, R., BRIAIS, A., BROWN, E. A., CHEN, Y., CLIFT, P. D., COLWELL, F. S., DADD, K. A., DING, W., ALMEIDA, I. H., HUANG, X.-L., HYUN, S., JIANG, T., KOPPERS, A. A. P., LI, Q., LIU, C., LIU, Z., NAGAI, R. H., PELEO-ALAMPAY, A., SU, X., TEJADA, M. L. G., TRINH, H. S., YEH, Y.-C., ZHANG, C., ZHANG, F. & ZHANG, G.-L. 2014. Ages and magnetic structures of the South China Sea constrained by deep tow magnetic surveys and IODP Expedition 349. *Geochemistry, Geophysics, Geosystems* **15**, 4958–83.

LIOU, J. G. 1979. Zeolite facies metamorphism of basaltic rocks from the East Taiwan Ophiolite. *American Mineralogist* **64**, 1–14.

LIOU, J. G. & ERNST, W. G. 1979. Oceanic ridge metamorphism of the East Taiwan Ophiolite. *Contributions to Mineralogy and Petrology* **68**, 335–48.

LIOU, J. G., LAN, C. Y., SUPPE, J. & ERNST, W. G. 1977. *The East Taiwan Ophiolite – its occurrence, petrology, metamorphism and tectonic setting, Taipei, Taiwan*. Taipei: Mining Research and Service Organization Industrial Technology Research Institute.

LUDWIG, K. R. 2003. *User's Manual for Isoplot/Ex, Version 3.0: A Geochronological Toolkit for Microsoft Excel*. Berkeley Geochronology Center Special Publication vol. 4.

MCDONOUGH, W. F. & FREY, F. A. 1989. Rare earth elements in upper mantle rocks. In *Geochemistry and Mineralogy of Rare Earth Elements* (eds B. R. Lipin & G. A. McKay), pp. 99–145. The Mineralogical Society of America, Reviews in Mineralogy 21.

MILSOM, J. 2003. Forearc ophiolites: a view from the western Pacific. In *Ophiolites in Earth History* (eds Y. Dilek & P. T. Robinson), pp. 507–15. Geological Society of London, Special Publication no. 218.

MULLEN, E. D. 1983. $MnO/TiO_2/P_2O_5$: a minor element discriminant for basaltic rocks of oceanic environments and its implications for petrogenesis. *Earth and Planetary Sciences Letters* **62**, 53–62.

PAGÉ, B. M. & SUPPE, J. 1981. The Pliocene Lichi mélange of Taiwan: its plate-tectonic and olistostromal origin. *American Journal of Science* **281**, 193–227.

PEARCE, J. A. 2003. Supra-subduction zone ophiolites: the search for modern analogues. In *Ophiolite Concept and the Evolution of Geological Thought* (eds Y. Dilek Y & S. Newcomb), pp. 269–93. Geological Society of America Special Paper no. 373.

PEARCE, J. A. 2014. Immobile element fingerprinting of ophiolites. *Elements* **10**, 101–8.

PEARCE, J. A., LIPPARD, S. J. & ROBERTS, S. 1984. Characteristics and tectonic significance of supra-subduction zone ophiolites. In *Geology of Marginal Basins* (eds P. Kokelaar & M. Howells), pp. 77–94. Geological Society of London, Special Publication no. 16.

PETERS, T. & MERCOLLI, I. 1998. Extremely thin oceanic crust in the proto-Indian Ocean: evidence from the Masirah ophiolite, Sultanate of Oman. *Journal of Geophysical Research* **103**, 677–89.

PRINZHOFER, A. & ALLEGRE, C. J. 1985. Residual peridotites and the mechanisms of partial melting. *Earth and Planetary Science Letters* **74**, 251–65.

PUBELLIER, M., GARCIA, F., LOEVENBRUCK, A. & CHOROWICZ, J. 2000. Recent deformation at the junction between the north Luzon block and the central Philippines from ERS-1 images. *Island Arc* **9**, 598–610.

STERN, R. J. & BLOOMER, S. H. 1992. Subduction zone infancy: examples from the Eocene Izu-Bonin-Mariana and Jurassic California arcs. *Geological Society of America Bulletin* **104**, 1621–36.

SUN, S. S. & MCDONOUGH, W. F. 1989. Chemical and isotopic systematics of oceanic basalts: implications for mantle composition and processes. In *Magmatism in the Ocean Basins* (A. D. Saunders & M. J. Norry), pp. 313–45. Geological Society of London, Special Publication no. 42.

SUPPE, J. 1984. Kinematics of arc-continent collision, flipping of subduction, and back-arc spreading near Taiwan. *Memoir of the Geological Society of China* **6**, 21–33.

SUPPE, J. & LIOU, J. G. 1979. Tectonics of the Lichi Mélange and East Taiwan Ophiolite. *Memoir of the Geological Society of China* **3**, 147–53.

SUPPE, J., LIOU, J. G. & ERNST, W. G. 1981. Paleogeographic origins of the Miocene East Taiwan Ophiolite. *American Journal of Science* **281**, 228–46.

TAPPONNIER, P., LACASSIN, R., LELOUP, P. H., SCHÄRER, U., ZHONG, D. L., WU, H. W., LIU, X. H., JI, S. C., ZHANG, L. S. & ZHONG, J. Y. 1990. The Ailao Shan-Red River metamorphic belt: tertiary left-lateral shear between Indochina and South China. *Nature* **343**, 431–7.

TAYLOR, B. & HAYES, D. E. 1980. The tectonic evolution of the South China Basin. In *The Tectonic and Geologic Evolution of Southeast Asian Seas and Islands* (ed. D. E. Hayes), pp. 89–104. American Geophysical Union, Geophysical Monograph vol. 23. Washington, DC, USA.

TAYLOR, B. & HAYES, D. E. 1983. Origin and history of the South China Sea basin. In *The Tectonic and Geologic Evolution of Southeast Asian Seas and Islands: Part* **2** (ed. D. E. Hayes), pp. 23–56. American Geophysical Union, Geophysical Monograph vol. 27. Washington, DC, USA.

TENG, L. S. 1987. Stratigraphic records of the late Cenozoic Penglai orogeny of Taiwan. *Acta Geologica Taiwanica Science Reports of National Taiwan University* **25**, 205–24.

TENG, L. S. 1990. Geotectonic evolution of the late Cenozoic arc-continent collision in Taiwan. *Tectonophysics* **183**, 57–76.

TENG, L. S. 1996. Extensional collapse of the northern Taiwan mountain belt. *Geology* **24**, 949–52.

TENG, L. S. 2007. *Quaternary Tectonics of Taiwan*. Central Geological Survey Special Publication 18, 24 pp.

TENG, L. S. & LIN, A. T. 2004. Cenozoic tectonics of the China continental margin: insights from Taiwan. In *Aspects of the Tectonic Evolution of China* (eds J. Malpas, C. J. N. Fletcher, J. Ali & J. C. Aitchison), pp. 313–32. Geological Society of London, Special Publication no. 226.

TSAI, Y. B. 1986. Seismotectonics of Taiwan. *Tectonophysics* **125**, 17–37.

WAKABAYASHI, J. & DILEK, Y. 2003. What constitutes 'emplacement' of an ophiolite?: mechanisms and relationship to subduction initiation and formation of metamorphic soles. In *Ophiolites in Earth History* (eds Y. Dilek & P. T. Robinson), pp. 427–47. Geological Society of London, Special Publication no. 218.

WHATTAM, S. A. & STERN, R. J. 2011. The 'subduction initiation rule': a key for linking ophiolites, intra-oceanic forearcs, and subduction initiation. *Contributions to Mineralogy and Petrology* **162**, 1031–45.

XIA, B., CUI, X. J., ZHANG, Y. H., LIU, B. M., WANG, R. & YAN, Y. 2005. Dynamic factors for the opening of South China Sea and a numerical modeling discussion. *Geotectonica et Metallogenia* **29**, 328–33.

YUMUL JR., G. P., DIMALANTA, C. B., TAMAYO JR., R. A. & MAURY, R. C. 2003. Collision, subduction and accretion events in the Philippines: a synthesis. *Island Arc* **12**, 77–91.

ZHANG, J., XIONG, L. P. & WANG, J. Y. 2001. Characteristics and mechanism of geodynamic evolution of the South China Sea. *Chinese Journal of Geophysics* **44**, 602–10.

ZHU, B. Q., WANG, H. F., CHEN, Y. W., CHANG, X. Y., HU, Y. G. & XIE, J. 2004. Geochronological and geochemical constraint on the Cenozoic extension of Cathaysian lithosphere and tectonic evolution of the border sea basins in East Asia. *Journal of Asian Earth Sciences* **24**, 163–75.